

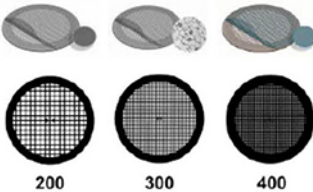
# Nanocharacterization by TEM and AFM

We offer a wide range of TEM and AFM tools, from TEM grids and finders to AFM substrates and grippers.

Available in a wide variety of designs and materials to support your work, select from a broad range of mesh sizes, specimen supporting films, and materials that perfectly suit the conditions of your TEM analysis.

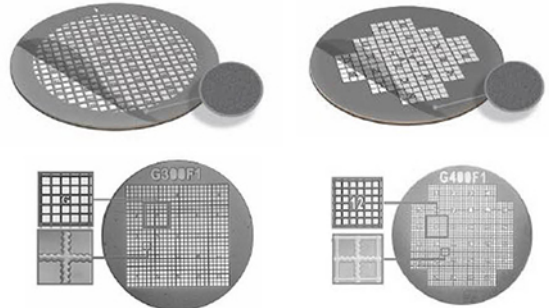
## TEM grid specifications:

Material	Mesh Size and Shape	Film Specifications
<ul style="list-style-type: none"> <li>Cu</li> <li>Ni</li> <li>Au</li> <li>Mo</li> <li>Cu/Pd</li> </ul>	<ul style="list-style-type: none"> <li>Square or hexagonal</li> <li>Single-hole grid (75 mm or 100 mm)</li> <li>100</li> <li>150</li> <li>200</li> <li>300</li> <li>400</li> </ul>	<ul style="list-style-type: none"> <li>None</li> <li>Continuous formvar film (thicknesses: 5-6 nm, 10 nm)</li> <li>Lacey carbon film (average hole sizes: 50 nm, 100 nm, 150 nm, 100 nm, 150 nm)</li> <li>Continuous amorphous carbon film (thicknesses: 10 nm, 20-30 nm)</li> <li>Continuous formvar/carbon film (thickness: 10nm formvar and 1nm carbon)</li> </ul>



## TEM finder grid specifications:

Material	Mesh Size	Film Specifications
<ul style="list-style-type: none"> <li>Cu</li> <li>Ni</li> <li>Au</li> </ul>	<ul style="list-style-type: none"> <li>135</li> <li>200</li> <li>300</li> <li>400</li> </ul>	<ul style="list-style-type: none"> <li>None</li> <li>Continuous amorphous carbon film (thicknesses: 3-4 nm, 10 nm, 20-30 nm)</li> </ul>



## Supporting Tools for Nanomaterial Characterization

Our comprehensive range of supporting materials for nanomaterial characterization includes tweezers (sharp tip, disc gripper for AFM), TEM window grids (various thicknesses, 1 or 9 windows), a magnetic pick-up tool, a grid storage box, cryo-capsules, lift-out grids (Cu or Mo), AFM substrates (various dimensions), and much more.



Explore our complete range of TEM grids on: [SigmaAldrich.com/nanocharacterization](https://SigmaAldrich.com/nanocharacterization)

© 2022 Merck KGaA, Darmstadt, Germany and/or its affiliates. All Rights Reserved. Merck, the vibrant M, and Sigma-Aldrich are trademarks of Merck KGaA, Darmstadt, Germany or its affiliates. All other trademarks are the property of their respective owners. Detailed information on trademarks is available via publicly accessible resources.

MK\_AD9792EN 43729 08/2022

The Life Science business of Merck operates as MilliporeSigma in the U.S. and Canada.

# Simulation of Structure Formation during Drying of Lithium-Ion Battery Electrodes using Discrete Element Method

Mark Lippke,\* Tobias Ohnimus, Thilo Heckmann, Dimitri Ivanov, Philip Scharfer, Wilhelm Schabel, Carsten Schilde, and Arno Kwade


Lithium-ion batteries are state-of-the-art and still their performance is subject to constant improvement. These enhancements are based, among other things, on optimization in the electrode production process chain. High optimization potential exists for the drying process of electrodes, as aiming for high drying speeds can greatly reduce both, investment costs and operating costs of the drying. However, high drying rates without appropriate precautions go hand in hand with poorer cell performance and adhesive strength, leading to a conflict between the required performance and production costs of the electrodes. Herein, a numerical approach based on the discrete element method to describe the formation of the electrode structure during drying is presented. The focus is placed on the active material structure and the effects due to particle interactions. Herein, a direct numerical description of the fluid phase is avoided by using various fluid substitute models, so that the simulation time and the computational costs can be greatly reduced. The model is validated by simulating different electrode areal loadings and comparing the achieved layer thicknesses to experimental results of the electrode drying process. A high agreement between experiment and simulation regarding density is obtained for different areal loadings.

## 1. Introduction

In the course of the development toward a CO<sub>2</sub>-neutral society, high-performance batteries play a central role. The demand for the

M. Lippke, T. Ohnimus, D. Ivanov, C. Schilde, A. Kwade  
Institute for Particle Technology  
Technical University Braunschweig  
38104 Braunschweig, Germany  
E-mail: m.lippke@tu-braunschweig.de

T. Heckmann, P. Scharfer, W. Schabel  
Thin Film Technology (TFT)  
Karlsruhe Institute of Technology (KIT)  
76131 Karlsruhe, Germany

 The ORCID identification number(s) for the author(s) of this article can be found under <https://doi.org/10.1002/ente.202200724>.

© 2022 The Authors. Energy Technology published by Wiley-VCH GmbH. This is an open access article under the terms of the Creative Commons Attribution-NonCommercial-NoDerivs License, which permits use and distribution in any medium, provided the original work is properly cited, the use is non-commercial and no modifications or adaptations are made.

DOI: 10.1002/ente.202200724

performance of batteries is continuously increasing. In addition to the optimization of the cell design and the use of more efficient materials, the optimization of individual processes in electrode production as well as the interaction of the individual process steps represent a major lever to meet the increasing demands on batteries.<sup>[1]</sup>

For example, a wide variety of studies show that the performance of battery electrodes could be greatly influenced by the targeted optimization of individual process steps such as dispersing,<sup>[2–5]</sup> drying,<sup>[5–8]</sup> and calendering.<sup>[9–11]</sup>

A central role in the drying of lithium-ion electrodes plays the binder segregation, which occurs particularly at high drying rates and high areal loadings. This phenomenon is associated with poorer adhesive strength of the electrodes and inferior electrochemical performance<sup>[8,12]</sup> and is in contradiction to industrially targeted high drying rates. A possible solution is to use different drying rates at different

times of the drying process.<sup>[6]</sup> There are various approaches for modeling binder segregation, which are essentially based on the solution of diffusion-convection equations and able to make statements about the average binder concentration over the electrode layer height.<sup>[13]</sup> The advantage of this approach is that it offers a very fast and in comparison with 3D-resolved models simple method to gain knowledge on the binder distribution and the effect of various process parameters on it.

For modeling the active material structure, coarse-grained molecular dynamics (CGMD) approaches exist.<sup>[14–18]</sup> Here, the active material is modeled according to a given particle size distribution. For inactive material, a surrogate material (carbon binder domain, CBD) is defined, which represents carbon black, binder, and solvent. During the drying process, this surrogate material shrinks under NPT (isothermal–isobaric ensemble) conditions, which is supposed to represent the evaporation of the solvent. Validation of the particle interactions takes place via the simulative determination of the rheological slurry behavior. In later publications, an approach is presented to map binder migration through locally different shrinkage rates of the inactive material particles.<sup>[19]</sup> Capillary effects are mimicked by increasing the attractive force fields in sections with lower remaining

solvent contents. Using this approach, a deep study of the influence on the drying rate on the electrode microstructure and the inactive material distribution is carried out, which is in good agreement with the experimental findings of Jaiser<sup>[6]</sup> regarding the effects of variations of the drying rate during the drying process. A major advantage over analytical approaches like the one of Font<sup>[13]</sup> is the possibility to obtain 3D distribution instead of 1D distribution. Also, numerous works<sup>[16,17,20]</sup> regarding coupling approaches of the CGMD-based drying simulations with calendaring simulations exist, that are able to map the influence of different process parameters and electrode formulations on the electrode structure and the electrochemical performance.

An approach presented by Srivastava<sup>[21]</sup> summarizes the carbon black particles and the binder phase as carbon black binder domain particles; in contrast to the approaches presented so far, these particles do not contain solvent. The influence of solvent evaporation is reproduced by compressing the particles from the top and not by changing the size of the CBD particles. Afterward, a uniaxial compression step representing the calendaring process is carried out. This workflow was the basis for a deep study on the influence of the cohesion and adhesion strength of the binder on the transport properties of the electrode mesostructure.

In the following, a discrete element method (DEM) approach will be presented that places greater focus on modeling more explicitly the individual effects which influence structure formation at the particulate level. This is intended to provide a basis that can easily be extended later with models for the development of binder distribution during drying, as well as even more accurate contact models, and allows coupling with the calendaring model by Sangros et al.<sup>[22–24]</sup> An advantage of the presented approach is that the main fluid effects like Stokes friction, buoyancy, lubrication, and capillary forces could be adequately represented by corresponding surrogate models without using computational fluid dynamics (CFD) simulation, thus saving a lot of computational power or time compared with coupled CFD–DEM simulations. In addition, an approach was developed that makes it possible to greatly accelerate the simulation and, thus, to simulate a microparticulate process over several hours.

## 2. Theory of Drying

The drying of electrode slurries can be divided into three drying phases, which can be distinguished by their respective drying rates. In the initial so-called constant rate period (CRP), a constant evaporation rate of the solvent exists, which results in a constant rate of decrease in the wet film thickness. With progressive drying, the average spacing of the particles within the suspension decreases. Finally, the active material particles form a self-supporting structure, so that the layer height does not show any significant decrease from this point onward.<sup>[7]</sup> Afterward, the liquid level no longer sinks horizontally and evenly. Instead, initially larger pores and then subsequently smaller pores are emptied further with increasing drying.<sup>[25]</sup> Shortly after the final layer thickness is reached, the drying rate decreases. This is characteristic for the second drying phase, the so-called falling rate period. However, various studies have shown that even after the final layer thickness is reached, a constant drying rate can

continue for a longer period of time, provided that the diffusion resistance for solvent transport within the electrode is relatively low.<sup>[6]</sup> During the third drying stage, residual moisture desorbs from the electrode structure until it reaches the sorption equilibrium.<sup>[26]</sup>

From an economic point of view, the aim is to achieve the fastest possible drying process. However, a high drying speed is generally associated with significant binder and carbon black migration. This has negative effects on the electrochemical performance as well as the mechanical integrity of the electrode.<sup>[7,8,12]</sup> A higher drying rate with consistent electrode quality can be achieved by selectively adjusting the drying rate during the drying process.<sup>[6]</sup> There are various approaches for modeling binder segregation, which are mainly based on the solution of diffusion–convection equations (Equation (1)) and are able to make statements about the average binder concentration over the height.<sup>[13]</sup>

$$J = Fc - D_{\text{eff}} \frac{\partial c}{\partial z} \quad (1)$$

where  $J$  represents the volume-averaged flow of dissolved binder. The convective flow is represented by  $F$ , whereas  $c$  corresponds to the concentration of the dissolved binder in the solvent and  $D_{\text{eff}}$  corresponds to the effective diffusion coefficient of the dissolved binder in the slurry, which is used to calculate the diffusion flux along the layer height  $z$ .

In the following sections, the forces acting on the solid particles will be examined to identify the relevant forces for a simulative representation of the drying process. A distinction can be made between interparticulate forces such as van der Waals forces and forces that are not based on particle interactions, such as an external gravity field.

## 3. Interparticulate and Fluid–Particle Interactions

Van der Waals forces play a central role in microparticulate systems. In addition to these attractive van der Waals forces, repulsive electrostatic forces as a part of the DLVO theory exist, which are based on the fact that particles can carry charges on their surfaces.<sup>[27]</sup> This results in the formation of a layer of oppositely charged fluid ions. When two particles approach each other, a superposition of these ion layers occurs and, with it, a repulsive force. In the context of cathode slurries, Zhu et al.<sup>[28]</sup> showed that the van der Waals forces clearly dominate electrostatic repulsion.

In addition to the previously mentioned effects of the DLVO theory, steric effects due to the use of polymers as binders would also be conceivable. In this case, polymers adsorb on the particle surfaces. If two particles approach each other, there is a depletion of solvent in the overlapping area of the polymer shell, which results in an osmotic pressure, which causes a repulsive force on the particles. In addition, there are entropic phenomena.<sup>[29]</sup> Cathode suspensions such as those considered in the following typically use *N*-methyl-2-pyrrolidone (NMP) as the solvent and polyvinylidene fluoride (PVDF) as the binder. For the PVDF/NMP system, however, Sung et al. showed that PVDF within a suspension binds neither to the active material [lithium-nickel-manganese-cobalt-oxide (NCM)] nor to the carbon black

and no steric effects can be observed.<sup>[30]</sup> They come to the conclusion that in the investigated system PVDF only raises the matrix viscosity and does barely affect the NCM–CB network. However, for slightly different systems (LiCoO<sub>2</sub> instead of NCM), Cho et al. and Kwon et al. observed an aggregation of binder and carbon black within a time span of numerous days.<sup>[31,32]</sup> For anodes, Ishii et al.<sup>[33]</sup> reported significant changes in the fundamental rheological behavior of the slurries for slightly different binder concentrations. These results demonstrate that the interactions in each slurry composition can be significantly different even for small variations in composition. Therefore, the behavior observed by Sung et al.<sup>[30]</sup> was used as a basis, as it offers the biggest match regarding the composition with the model suspension used in this study. For other material systems like anodes for example the model presented by Ma et al.<sup>[29]</sup> could be used to depict steric effects.

In addition, displacement effects should be considered: If two particles approach each other, the solvent localized between them must be displaced, which exerts a repulsive force on both particles. In the following sections, these forces are referred to as lubrication forces.<sup>[34]</sup>

In addition to the named interparticulate forces, the particles experience a weight force and a hydrostatic buoyancy force as a result of gravity. The movement of the particles is slowed down by viscous friction in the surrounding fluid. Due to the low sedimentation velocities, Stokes friction is assumed. In addition to the sedimentation of the particles, the sinking of the fluid surface plays a central role, as particles are dragged along by the fluid interface.

For active materials, a significant influence of diffusion effects is neglected due to the comparably large particle size and the high viscosity of the binder solution.

#### 4. Drying Model

The presented model is based on the DEM, which models particle motion using Newtonian equations of motion.<sup>[35]</sup> The particle size distribution of NCM was measured via laser diffraction (Horiba LA-960) (Figure 1). As laser diffraction measurements are prone to broaden the particle size distribution,<sup>[36,37]</sup> the top and bottom 15% of the distribution were ignored. The remaining 70% of the distribution is discretized using five representative sizes classes with the same volume fraction (6.5, 7.58, 8.6, 9.82, and 11.35 μm).

Within a battery suspension, the particle size distribution of carbon black is bimodal consisting of smaller aggregates (≈200–500 nm) and coarser agglomerates (≈2–5 μm). As the size scale between the active material particles and the carbon black aggregates differs greatly (approximately by a factor of 10–20), carbon black particles are represented by spheres with a diameter of 1.5 μm to keep the computational effort feasible. Because of the attractive van der Waals interactions, those carbon black (CB) particles are able to form agglomerates. In preliminary studies, the influence of smaller CB diameters was investigated. This required smaller time steps and readjustment of the cut-of-distances for the van der Waals model and friction parameters but resulted in comparable results.

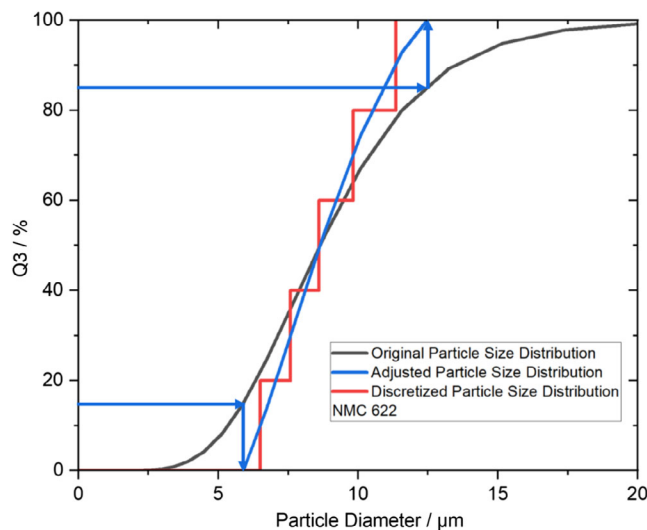


**Figure 1.** Particle size distribution of NCM 622 measured using laser diffraction (gray). The smallest and coarsest 15% of size distribution are neglected and the size distribution is adjusted (blue). The discretized size distribution for the DEM simulation is depicted in red.

Various studies have shown that the carbonblack–binder network can have a strongly varying porosity depending on the process route.<sup>[3,38]</sup> This value can be correlated with the porosity of carbon black. Bockholt and Mayer<sup>[3,38]</sup> investigated the influence of the wet and dry mixing processes on the carbon black–binder network porosity and developed a method to determine it using mercury intrusion measurements. The method distinguishes between the larger pores between the active material particles and smaller pores within the carbon black–binder network. The porosity of the carbon black binder network can be determined using the porosity of the larger pores  $\epsilon_{C,NMC}$ , the total porosity  $\epsilon_C$  of the entire coating, and the solid volume fraction of NMC  $C_{v,NMC}$  in the coating.

$$\epsilon_{CB} = \frac{\epsilon_C - \epsilon_{C,NMC}}{1 - C_{v,NMC} - \epsilon_{C,NMC}} \quad (2)$$

It was found that long and especially intensive dry mixing processes can strongly reduce the carbon black–binder network porosity. Higher process intensity in wet mixing also led to lower carbon black–binder network porosities, but the influence was significantly lower. Overall, carbon black–binder network porosities of about 0.3–0.8 could be measured. In the high-intensity dry mixing processes, it was also observed that carbon black was coated onto the active material particles.<sup>[3,38]</sup>

The influence of the carbon black–binder network porosity is modeled in the presented approach using a higher number of carbon black particles. As the carbon black can only be depicted by dense, monodispersed particles in the DEM simulation, the only way to mimic the effect of the internal porosity of the carbon black is by increasing the number of these particles. The ingested volume does not change as the density of the carbon black particles is adjusted in parallel so that the inserted mass also stays constant. The coating of the active material with carbon black can

be represented by increasing the diameter of the active material if needed.

Furthermore, it should be noted that the porosities of the carbon black–binder network determined according to Mayer and Bockholt<sup>[38]</sup> may have to be increased for the simulative replication of electrodes because carbon black agglomerates can have a highly branched appearance and, thus, form significantly more porous structures than a packing of spheres of the same volume could.

The shape of typical carbon black aggregates and agglomerates and the fact that the carbon black can only be represented as spheres in the model are the reasons why friction coefficients containing carbon black as a friction partner should be adjusted and treated as calibration parameters to achieve the same process behavior as in the coating and drying experiments. Form closures in the ramifications of carbon black, aggregates and agglomerates can lead to a hooking of the particles with each other, which could only be mapped within the simulation by accordingly high friction coefficients.

It should also be noted that the usual determination procedures for friction coefficients cannot be applied in the case of drying battery slurries. A common methodology would include measurements of the static and dynamic angle of repose. The results would then be used as target parameters for calibration simulations.<sup>[39]</sup> However, as it can be assumed that the wet and dry mixing process taking place beforehand strongly alters the carbon black structure, the use of measurement data obtained on unprocessed carbon black would not make sense. Consequently, a different approach for the calibration of the friction parameter must be selected.

Taking into account their mass fraction in the formulation, the particles are randomly placed in a simulation box with a base area of  $75 \times 75 \mu\text{m}^2$ , assuming periodic boundary conditions parallel to the base area. The height of the simulation box corresponds to the wet film thickness, which can be calculated according to Equation (3) and (4), if the areal loading of the dried electrodes and the mass fraction of solvent in the suspension are known.

$$H_{\text{wet}} = \frac{L_{\text{Dry}}}{c_s} \left( \frac{x_f}{\rho_f} + \frac{x_s}{\rho_s} \right) \quad (3)$$

$$\rho_s = \left( \frac{c_{\text{NMC}}}{\rho_{\text{NMC}}} + \frac{c_{\text{PVDF}}}{\rho_{\text{PVDF}}} + \frac{c_{\text{CB}}}{\rho_{\text{CB}}} \right)^{-1} \quad (4)$$

The areal loading of the dried electrode is described by the weight  $L_{\text{Dry}}$ ;  $x_f$  and  $x_s$  correspond to the mass fractions of the fluid and the solids in the suspension. The density of the solvent used is depicted by  $\rho_f$ , whereas  $\rho_s$  is equivalent to the average solid's density, which can be determined with the help of the densities and mass fractions of the solid mixture of the individual components.

The particles interact with each other through van der Waals forces.<sup>[40]</sup> Equation (5) depicts a simplified form for the van der Waals forces assuming that  $R \ll r_j$  or  $r_i$  applies

$$F_{\text{vdW}} = - \frac{A_{ij} r_i r_j}{(r_i + r_j) \cdot 6R^2} \quad (5)$$

where  $r_i$  and  $r_j$  represent the radii of particles  $i$  and  $j$ , where the distance between the particles is defined as  $R$ . The Hamaker constant to be applied for the interactions is  $A_{ij}$ . To reduce the computational cost, a maximum distance is set, as suggested by Zhu,<sup>[28]</sup> beyond which no van der Waals forces are computed, as these are very small for larger particle distances. As the van der Waals forces tend toward infinity for decreasing particle–particle distances, a minimum particle–particle distance must be defined to ensure numerical stability. If the particle-to-particle distance falls below this minimum, the minimum particle-to-particle distance is used to calculate the van der Waals forces. The minimum distances chosen are 50 nm (NMC–NMC), 5 nm (CB–CB), and 10 nm (NMC–CB).

As the intended model shall be based on a pure DEM consideration, all fluid effects must be represented by corresponding substitute models.

The lubrication forces mentioned in the beginning are represented with the help of the model of Kroupa et al.,<sup>[34]</sup> who used the complete framework collected by Dance and Maxey.<sup>[41]</sup> They derived equations for particle–particle and particle–wall interactions for which the flow between single particles is in the Stokes' limit. Lubrication forces occur when two particles move toward or away from each other. Fluid is displaced or attracted by the process. This provides a dissipative force, which was used for the normal direction between two particles in this work as follows

$$\mathbf{F}_{\text{nl}} = -6\pi r \cdot \eta_{\text{Liquid}} \cdot v_r \cdot \mathbf{n} \left( \frac{1}{4} \kappa^{-1} - \frac{9}{40} \log(\kappa) - \frac{3}{112} \kappa \log(\kappa) \right) \quad (6)$$

In this equation,  $\kappa = h/r$  is the relative distance, with  $h$  is the distance between the surfaces, and  $v_r = v_i - v_j$  is the relative velocity of the particles  $i$  and  $j$ . The unit normal vector  $\mathbf{n}$  points from the center of particle  $i$  to the center of particle  $j$ . The equations for the tangential force as well as, the sliding and twisting torque used in this work can be taken from literature.<sup>[34]</sup>

As the equations for the lubrication force diverge for  $\kappa \rightarrow 0$  to infinity, Vinogradova<sup>[42]</sup> proposed a correction factor  $f^*$  defined as

$$f^* = \frac{h}{3h_c} \left[ \left( 1 + \frac{h}{6h_c} \right) \cdot \ln \left( 1 + \frac{6h_c}{h} \right) - 1 \right] \quad (7)$$

with the critical slip length  $h_c = \kappa_c \cdot r$ . This equation is multiplied with the right-hand side of Equation (6). As long as  $h$  is higher than  $h_c$ , the real surface distance  $h$  is used. As soon as the particles are closer than  $h_c$ , a fixed value of  $\kappa_c = 0.1$  for the relative distance and  $h = h_c$  for the absolute distance is used. Kroupa et al.<sup>[34]</sup> showed that this value is optimal to match the viscosity of a suspension with the Krieger–Dougherty model. Without this method, particles would not be able to touch each other. The force is also cut off for the distance between particle surface  $h$  higher than the particle radius  $r$ , because otherwise there would be a change of the sign of the parts in the equation with the logarithms. Kroupa et al.<sup>[34]</sup> showed that this has only a small effect on the viscosity of the suspension because the force gets smaller with higher distances.

As described earlier, the sedimentation behavior of the particles is described by the interaction of buoyancy forces  $F_b$ , weight forces  $F_g$ , and viscous friction forces  $F_{Fr}$

$$F_g = \frac{4}{3}\pi \cdot r^3 \cdot \rho_{\text{solid}} \cdot g \quad (8)$$

$$F_b = \frac{4}{3}\pi \cdot r^3 \cdot \rho_{\text{Liquid}} \cdot g \quad (9)$$

$$F_{Fr} = 6\pi \cdot r \cdot \eta \cdot v \quad (10)$$

where  $r$  represents the radius of the particle under consideration with the density  $\rho_{\text{solid}}$ . The acceleration due to gravity is depicted by  $g$ . In the case of viscous friction,  $v$  represents the relative velocity between the fluid and the particles. For simplicity, it is assumed that the fluid is at rest and thus the velocity of the particle corresponds to the relative velocity between the particle and the fluid. The viscosity of the surrounding medium, which poses a complex question in the context of battery slurries, is depicted by  $\eta$ .

The viscosity of the suspension can be seen as the sum of various effects. The first part of the total viscosity is the viscosity of the solvent NMP, which is increased by the addition of PVDF. In addition, there is a strong increase in viscosity due to interparticle forces such as van der Waals forces, which is caused in particular by carbon black structures. This component shows strong shear-thinning behavior, as the carbon black superstructures are decomposed at higher shear rates. Also, there are volume effects, which are due to the fact that the solid's volume of the particles influences the flow behavior of the fluid. This effect can be described approximately by the Krieger–Dougherty model.<sup>[43,44]</sup>

As the shear-thinning effect of the carbon black interactions should at least be represented in the beginning by the van der Waals model and the volume effects are approximately reproduced by the lubrication model using the suspension viscosity, this would mean multiple representations of these effects. Therefore, for the viscosity of the surrounding medium  $\eta$  has assumed to be the viscosity of a PVDF-NMP suspension at a shear rate of  $0.01 \text{ s}^{-1}$ , as very low fluid and particle velocities are expected during the drying process.

The descending fluid level drags the particles along until they form a stable particle structure. The rate of descent is calculated in Section 6. This entrainment is due to a combination of pressure and capillary forces at the liquid surface. As the pressure forces can only be determined with the help of a high-resolution CFD simulation, we will limit ourselves to the capillary force as described by Breinlinger,<sup>[45]</sup> which is determined according to Equation (11) and applied as soon as a particle is in contact with the virtual fluid level.

$$F_{\text{cap}} = -2\pi\sigma \sin(\omega) \cdot \sin(\omega + \theta) \quad (11)$$

$$\omega = \arccos\left(\frac{-h_s}{r_i}\right) \quad (12)$$

where  $\sigma$  represents the surface tension between the fluid and the solid particles and  $\theta$  the corresponding contact angle. The wetting angle is described by  $\omega$  and is calculated using the particle radius  $r_i$  and the distance between the particle center and the liquid surface  $h_s$ .

To meet the constant evaporation rate of the CRP, the virtual liquid level is lowered at a constant speed. The entire simulation process is shown in Section 8.

#### 4.1. Scaling of Forces

The reduction of the simulation duration by several orders of magnitude represents a major challenge. The basic goal of simulating a microscale process lasting several minutes leads to unfeasible simulation durations without further scaling approaches. With scaling approaches known to the authors, such as those of Feng et al.,<sup>[46,47]</sup> which are based on similarity principles with regard to geometry, dynamics, and mechanics, it was not possible to achieve a stable simulation with an acceptable simulation duration, so that a different scaling approach was developed.

The fundamental idea of the approach is that the ratio of the stationary sinking velocity of the particles in relation to the fluid surface sinking velocity is kept constant.

$$\frac{v_{\text{FluidSurface;original}}}{v_{\text{Sedimentation;original}}} = \frac{v_{\text{FluidSurface;scaled}}}{v_{\text{Sedimentation;scaled}}} = \text{constant} \quad (13)$$

For this purpose, the relationships presented in Section 4 must be taken into account. If the simulation time is to be reduced by a factor of  $k$ , both the fluid surface descent rate and the stationary particle sinking rate must be increased by a factor of  $k$ . The fluid surface settling velocity can be set directly in the simulation. To adjust the stationary sinking rate of the particles, the gravitational constant can be scaled by the factor  $k$ . This adjusts the buoyancy and weight force. As the Stokes friction depends linearly on the particle velocity, no adjustments need to be made here.

One challenge is the interaction of the capillary forces of the liquid surface and the Stokes friction. With a desired scaling factor  $k$  of  $1 \times 10^7$ , this leads to an increase in Stokes friction by a factor of  $1 \times 10^7$ . For stability reasons, the capillary force can only be scaled with a scaling factor of about  $9 \times 10^3$ . Significantly higher scaling factors lead to too high particle overlaps and, therefore, result in numerical instable simulations. In the course of drying, the fluid surface pushes a steadily increasing amount of particles in front of it. On the one hand, these particles are pushed down by the liquid level, but at the same time, they receive a viscous frictional force against their direction of movement. This viscous frictional force increases with the amount of particles that the liquid level pushes, so that the frictional forces dominate the capillary force and the particles are pushed through the liquid surface without a continuous particle framework having formed. This is obviously unphysical and due to the incorrect scaling.

This problem can be overcome by reducing the viscosity used for the Stokes friction by a factor  $b$ . This has the unwanted effect of increasing the sinking speed of the particles by the factor  $b$ . To comply with the originally defined scaling criterion, the steady-state sinking velocity can be reduced by a factor  $b$  by reducing the gravitational constant. For  $b$ , a factor of 10 proved to be practicable.

To scale the van der Waals forces, the Hamaker constants for the pairings NMC–NMC, CB–NMC, and CB–CB were increased by a factor of  $1 \times 10^7$ .

Overall, it can be stated that the simulation time could be reduced by a factor of  $1 \times 10^7$ , which, however, is accompanied by losses in physical correctness. However, the generated results represent realistic behavior.

## 5. Experimental Section

The simulation approach was demonstrated using model electrodes. The following materials were used for the formulation shown  $\text{LiNi}_{0.6}\text{Co}_{0.2}\text{Mn}_{0.2}\text{O}_2$  (NCM 622, BASF), PVDF (PVDF 5130, Solvay), and carbon black (C Energy Super C65, Imerys) (CB). The formulation recipe is shown in **Table 1**.

### 5.1. Processing Route

The solid components of the formulation were mixed for 15 min at a rotational speed of  $49 \text{ m min}^{-1}$  in a tumbling drum mixer (TURBULA T2F, Willy A. Bachofen Corp.). The dry mixture was then suspended to a solid concentration of 70% using NMP and dispersed in a dissolver (Dispermat CA, VMA Getzmann) at a rotational speed of  $9 \text{ m s}^{-1}$ . After the dispersion process, the suspension was degassed for 30 min. More details can be taken from the study by Diener et al.<sup>[48]</sup>

The slurry was coated using a continuously operated pilot-scale coater/dryer (Kroenert, LabCo) with a combined comma-bar and reverse roll-coating system. Four different areal loadings were applied: 20.1, 25.2, 30.3, and  $35.4 \text{ mg cm}^{-2}$  (areal loadings refer to the dried electrode). The coated slurry was dried in a convective dryer consisting of three 2 m sections ( $T_1=80^\circ\text{C}$ ,  $T_2=100^\circ\text{C}$ , and  $T_3=120^\circ\text{C}$ ). In the first two sections, there was a diffuse inflow, whereas in the third section a direct inflow was used. The coating speed applied was  $2 \text{ m min}^{-1}$  for all the electrodes.

The carbon black–binder matrix porosity for the formulation was obtained by analyzing the areal loading of  $25.2 \text{ mg cm}^{-2}$ . A carbon black–binder matrix porosity of 0.506 was determined using Equation (2).

The mercury intrusion measurements were carried out using a PoreMaster PM 60GT (3P Instruments). More details regarding the test procedure can be taken from literatures.<sup>[38,49]</sup> The carbon black–binder porosities were obtained using the method of Mayer and Bockholt also described in Section 4.

## 6. Determination of Drying Rates

As described in Chapter 2, the drying process of a battery electrode can be divided into different drying phases. The first phase comprises the evaporation of the solvent from the film's surface or filled pores. During this first period, the drying rate is more or

**Table 1.** Overview of the formulation used.

	Mass fraction [wt%]
NMC 622	94
PVDF 5130	3
Carbon black	3

less constant and the film shrinks until it reaches its final thickness. The constant drying rate remains also beyond the end of film shrinkage, if enough filled pores face the surface.<sup>[25,50,51]</sup> The second drying phase starts as filled pores retreat from the surface and the mass transport resistance of the particle structure affects the evaporation. During the third drying period, residual moisture desorbs from the electrode until it reaches the sorption equilibrium.<sup>[26]</sup> The drying phenomenon of battery electrodes must be distinguished from the traditional three drying stages, because the transitions are spatially and temporarily distributed across the electrode.

The solvent evaporation can be modeled under knowledge of the drying rate, which is dependent on dryer characteristics and might also depend on film properties. In this study, the film shrinkage, which can be calculated from the drying rate, bridges the experimental drying conditions to the DEM simulation described in Section 4, ensuring an adequate implementation of the effects of the dryer's parameters. The interaction of the dryer with the solvent determines this drying rate, which can also be expressed as the film shrinkage as a function of time, until the drying electrode stops shrinking. In addition to the DEM simulation, the simulation of the dryer and the resulting drying rate and film shrinkage is predicted by a theoretical model according to Kumberg et al. This model takes properties of the dryer such as temperature and heat transfer coefficient as well as physical properties of the materials into account and calculates the propagation of drying inside the dryer. This calculation consists of 1D heat and mass transfer equations for the electrode.

$$\frac{dH_{\text{film}}}{dt} = \dot{Q}_{\text{top}} + \dot{Q}_{\text{bottom}} - \dot{H}_s(\dot{M}_s) \quad (14)$$

Equation (14) is the energy balance of the drying electrode.  $H_{\text{film}}$  is the enthalpy of the electrode that changes over time  $t$ . The heat fluxes  $\dot{Q}$  that reach the electrode from the top and bottom are a characteristic of the dryer and can be calculated by the heat transfer coefficient. The term  $\dot{H}_s$  represents the enthalpy flux of the evaporating solvent. This enthalpy flux is a function of the evaporating mass flow  $\dot{M}_s$  that can be described by the mass transport kinetics of the solvent in the gas phase.

Further details can be found in the publication of Kumberg et al. who developed this theoretical drying model and validated it via experiments for Li-ion battery anodes of varying thickness.<sup>[52,53]</sup> The model of Kumberg has been adapted to the drying of Li-ion battery cathodes by implementing appropriate material properties of solvent and electrode composition as well as characteristics of the dryer used (compare **Table A1**). Furthermore, feasible output parameters have been implemented for the transfer to the DEM simulation. **Figure 2** shows the results of the dryer simulation for an areal loading of the dried electrode of  $35.4 \text{ mg cm}^{-2}$ .

**Figure 2** plots the drying propagation over the length of the dryer. The  $y$ -axis on the left shows the film thickness and the secondary  $y$ -axis shows the temperatures of the film and dryer. **Figure 3** depicts the mass fraction of the solvent in the film during the drying process.

The film shrinks as soon as it enters the first dryer section and a linear shrinkage is achieved as soon as the steady-state

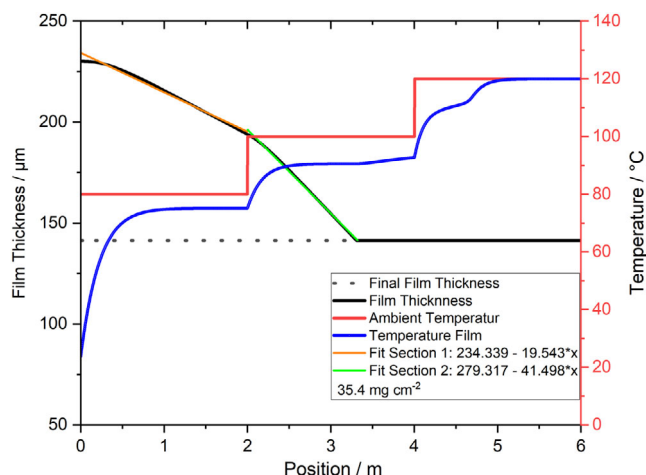


**Figure 2.** Propagation of the drying in the pilot-scale dryer. Each dryer section has a length of 2 m, an individual dryer temperature, as well as an individual heat transfer coefficient. The temperature of the film results from the equilibrium between ingoing energy and outgoing energy due to solvent evaporation. The film thickness decreases as the film shrinks until the particle network consolidates. This film shrinkage rate is linearly fitted and transferred to the DEM simulation.

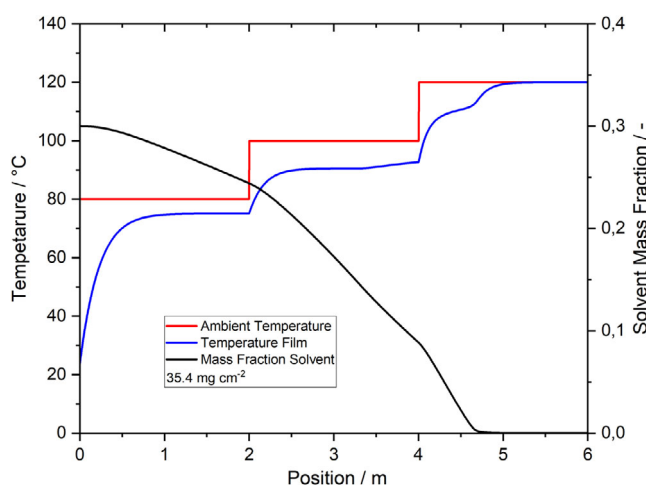


**Figure 3.** Temperature and solvent mass fraction of the film in the pilot-scale dryer calculated by the dryer model.

temperature of the first dryer section is reached. Upon entering the second dryer section, the propagation steepens and once again linearly shrinks as soon as the steady-state temperature of the second dryer section sets. As soon as the final film thickness is reached, the film thickness remains constant, while solvent evaporation continues. The temperature of the dryer is a step function, starting at 80 °C and increasing by 20 °C for each dryer section. The propagation of the film temperature starts at ambient temperature and increases to the steady-state temperature for each section. The film consolidates in the second dryer section. This consolidation affects the temperature propagation as the additional mass transport resistance of the porous structure decreases the drying rate and the film temperature rises

**Table 2.** Overview of the film shrinkage rates used for the different electrodes in each segment of the dryer (areal loading relates to the weight of the dried electrodes).

Electrode [mg cm <sup>-2</sup> ]	Section 1 [µm s <sup>-1</sup> ]	Section 2 [µm s <sup>-1</sup> ]	Section 3 [µm s <sup>-1</sup> ]
20.1	0.670	1.193	–
25.2	0.683	1.323	–
30.3	0.667	1.360	–
35.4	0.650	1.383	–

without any changes of the dryer temperature in this section. This phenomenon has been shown by Kumberg et al. for Li-ion battery anodes.<sup>[53]</sup> The verification of this phenomenon for this material system will be addressed in further studies. The film fully dries in the third section of the dryer. This can be concluded by the alignment of the film temperature to the dryer temperature, caused by the missing evaporation cooling of the solvent.

As a transfer parameter to the DEM simulation, the film shrinkage rate of each dryer section is linearly fitted and transferred to the DEM simulation. This transfer ensures a correct consideration of the dryer characteristics in the simulation.

The shrinkage rate depending on the position  $s_p$  is transferred into a time-dependent shrinkage rate  $s_t$  using the line speed  $v_l$

$$s_t = s_p \cdot v_l \quad (15)$$

An overview of the calculated film shrinkage rates is given in Table 2.

## 7. Simulation Parameters

For the NCM 622, Young's modulus of 142 GPa<sup>[22]</sup> as well as a density of 4.74 g cm<sup>-3</sup> were assumed. The Hertz–Mindlin contact model was used as the contact model. Although investigations by Sangros et al.<sup>[23]</sup> have shown that the Hertz–Mindlin contact model is not able to represent the mechanical behavior of NCM 622 particles at higher deformations, it is assumed that the mechanical particle behavior plays a negligible role in the drying process, so that the computationally less complex Hertz–Mindlin contact model can be considered as sufficient for drying simulations.

As the dry mixing processes were not highly intensive, it is assumed that the fraction of carbon black that has been coated onto the active material is negligible. Therefore, the diameter of the active material remains unchanged.

With regard to density, a density of 1.1875 g cm<sup>-3</sup> was used for CB agglomerates. This value takes into account the porosity of the CB particles, which is calibrated as shown in Section 9, ( $\rho_{CB} = 1.66 \text{ g cm}^{-3}$ )<sup>[54]</sup> and assumes that the pore volume is filled with NMP ( $\rho_{NMP} = 1.03 \text{ g cm}^{-3}$ ).<sup>[55]</sup>

For the surrounding fluid, a surface tension of 41 mN m<sup>-1</sup> was assumed,<sup>[55]</sup> which corresponds to the surface tension of NMP at 20 °C. As for the viscosity of the binder solution, temperature dependency was not taken into account. Moreover, a possible influence of PVDF on the surface tension was also neglected. As no data were available regarding the contact



angle of NMP to the particles, a contact angle of  $40^\circ$  was assumed.

Details of the carbon black porosity and the coefficient of friction can be found in Section 9.

The viscosity of an NMP–PVDF suspension with a PVDF content of 6.5 wt% was used at a shear rate of  $0.01 \text{ s}^{-1}$  (1.801 Pas), which means a slightly increased viscosity for a solid content of 70 wt%. However, these differences are negligible due to various other simplifications such as nonconsideration of temperature and binder gradients. Furthermore, the used viscosity values are subject to other assumptions anyway, as described earlier.

The original, unscaled Hamaker constants used are  $4.64 \times 10^{-20} \text{ J}$  (CB–CB),  $9.5 \times 10^{-19} \text{ J}$  (CB–NMC), and  $2.11 \times 10^{-19} \text{ J}$  (NMC–NMC).<sup>[28]</sup>

## 8. Simulation Procedure

After the simulation box was randomly filled with particles (Figure 4) as described in Section 4 and, thus, represents a completely mixed wet film, the virtual fluid level was lowered at the constant rate of descent determined according to Section 6. Within the process, the fluid level entrains active material and carbon black particles. Figure 5 shows the typical course of the liquid level and the layer thickness with increasing simulation time. The layer thickness corresponds to the highest upper edge of all particles and the expected linear decrease of the layer thickness can be seen. After 60 s, the coating leaves the first segment of the dryer. As the temperature in the second segment is 20 K higher than in the first segment, an increase in shrinkage rate can be observed.

Once a certain layer thickness is reached, the layer thickness does not decrease any further, while the liquid level continues to sink within the layer. The final layer thickness was assumed as soon as the layer thickness exceeded the liquid level by more than the diameter of the largest particle, because from this point on it can be definitely assumed that the particles lose contact with the liquid surface and, thus, the final layer thickness is reached (black dot in Figure 5). The following slight increase in the layer thickness is due to the fact that the upper particle layers increasingly experience no longer any force from the liquid level.

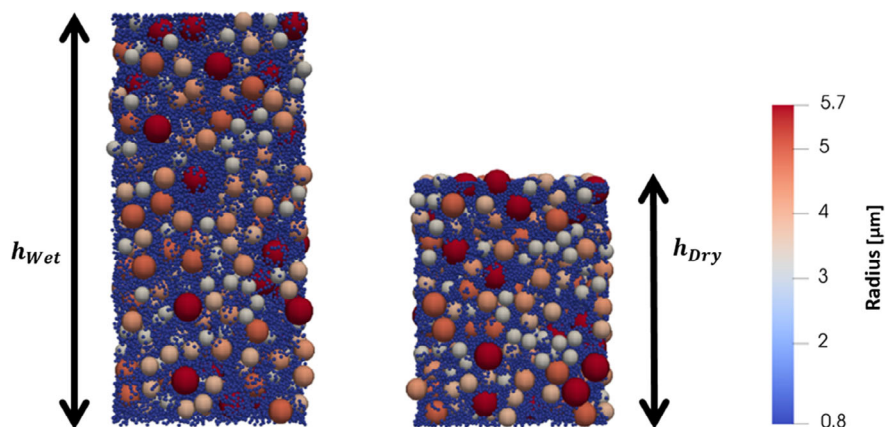


**Figure 4.** Exemplary wet film in the beginning of the simulation (left) and dried structure (right).

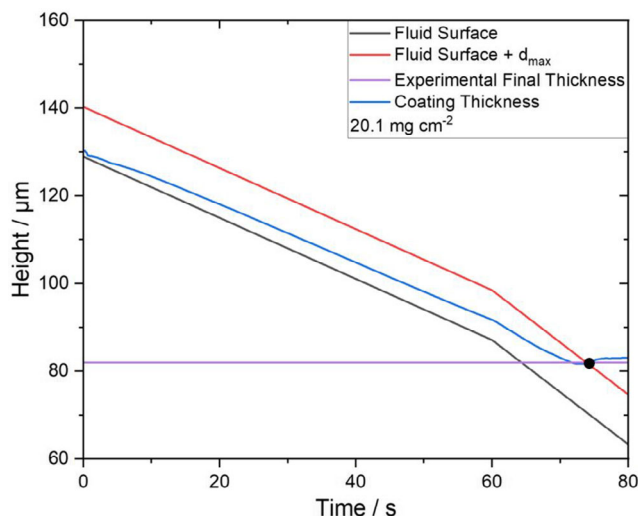


**Figure 5.** Development of the fluid surface and the coating thickness during the DEM drying simulation. The black dot marks the point, where a fixed coating thickness is assumed.

Consequently, a relaxation of these layers takes place, which results in an increase in the layer thickness. In reality, however, the liquid level does not sink further as a flat surface after reaching the final layer thickness, but rather a pore-by-pore evaporation of the remaining solvent takes place, which is not depicted in the simulation.<sup>[25]</sup>

As the dryer-orientated model presented in Section 6 needs the final layer thickness determined by the DEM simulation approach to provide the film shrinkage rates, but the DEM simulation needs the shrinkage rate calculated by the dryer-orientated model in the first place to determine the final layer thickness, an iterative approach using an initial guess for the final layer thickness has been deployed.

## 9. Results

The calibration and validation of the simulation approach are carried out using the previously presented dataset. For this purpose,

it is to be shown that by calibrating friction coefficients and carbon black porosities once using one areal loading, the layer thickness development can be correctly mapped as a function of the areal loading.

To calibrate the setup, the coefficient of friction and the carbon black porosity were varied first, as these two parameters had the highest influence on the final layer thickness in preliminary investigations. The coefficient of friction can only be considered as a calibration parameter due to the previously discussed experimental inaccessibility. Through a calibration study using the areal loading of  $20.1 \text{ mg cm}^{-2}$ , the coefficient of friction in this work was determined to a value of 0.8 for all material pairings. A distinction between the material pairings was not made for simplicity reasons. Furthermore, the simulations show that the carbon black agglomerates arrange themselves between the active material particles in such a way that direct contact between active material particles is mostly prevented and the equalization of the friction coefficients should not have a negative influence.

The porosity of the carbon black–binder network is estimated using the method presented by Mayer and Bockholt.<sup>[38]</sup> However, it is questionable to what extent the value obtained covers any shape influences of the carbon black agglomerates. Also, it has to be distinguished between the porosity of carbon black and of the carbon black–binder matrix. The carbon black–binder matrix determined by the method of Mayer and Bockholt should be used as an initial estimation for the carbon black porosity at the maximum for the reasons discussed in Section 4. Nevertheless, the basic considerations of Mayer and Bockholt can be adopted meaning that intensive dispersion and dry mixing processes should result in smaller carbon black porosities.

Thus, only the film thickness for one areal loading is required, based on which the friction coefficients and carbon black porosity are calibrated to predict, within the selected formulation and processing, the film thickness for any areal loading.

Through calibration studies, a carbon black porosity of 0.75 was determined for the modeled formulation. This value is higher than the one that was calculated for the carbon black–binder matrix porosity. However, these differences can be attributed to the reasons already discussed.

**Figure 6** shows the layer thickness and density obtained in experiment and simulation, respectively, for the different areal loadings. Every areal loading was simulated three times with different random initial particle positions. The standard deviations of the simulations were insignificantly low. With regard to the layer thickness, an almost perfect agreement can be seen for an areal loading of  $20.1 \text{ mg cm}^{-2}$ . This exceptionally high agreement is due to the fact that this data point was used for the calibration of the friction coefficients and the carbon black porosity. For the areal loadings of  $25.2$  and  $30.3 \text{ mg cm}^{-2}$ , a slight underestimation by the simulation can be detected. However, the agreement between simulation and experiment is very high. For the highest areal loading, the simulation slightly overestimates the layer thickness. However, the difference between simulation and experiment is within or at least almost within the standard deviation of the measurement points.

As both the porosity and the density of the coating are calculated directly from the coating thickness, there is very high agreement between the simulation and the experiment, and overall, the simulation depicts those experimental values very well.

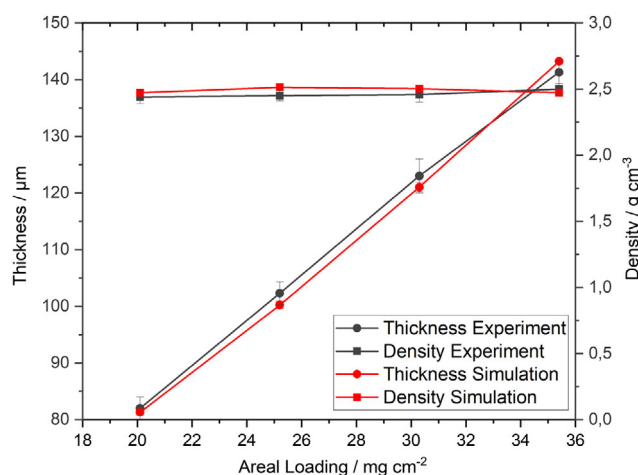


**Figure 6.** Thickness and density for different areal loadings.

In addition, the pore size distribution of the virtual structure with an areal loading of  $25.2 \text{ mg cm}^{-2}$  was also determined. The PoroDict 2021 module of the GeoDict software was used for this purpose. The chord lengths of the pores of the virtual structure were determined.

**Figure 7** shows a comparison of the measured and simulated pore size distribution. The peak of the experimental measurement shows an  $\approx 0.8 \mu\text{m}$  higher pore diameter. This difference can be attributed to the fact that the simulation simplifies the complex structure of the carbon black to coarse-grained mono-dispersed spheres. As discussed previously, due to the nonconsideration of the complex carbon black shape, the volume of carbon black might be overestimated by the calibration process. The thus possibly too high particle volume might lead to a reduction of the pore diameter.

Also noticeable is the very narrow and very high peak of the virtual pore size distribution. One reason for this might be the monodispersity of the carbon black particles used. As shown in Figure 4, the carbon black particles clearly dominate

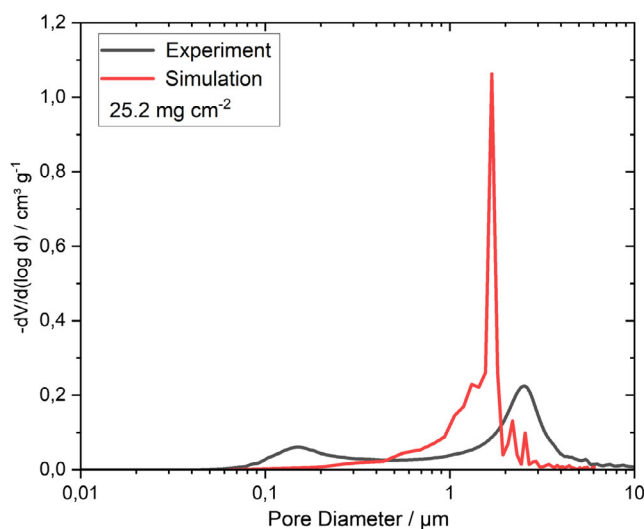


**Figure 7.** Pore size distribution for an areal loading of  $25.2 \text{ mg cm}^{-2}$ .

the pore structure. Therefore, the usage of monodispersed carbon black particles could explain the very narrow pore size distribution. This phenomenon should be investigated in further studies by applying particle size distributions for the carbon black.

Furthermore, unlike in the experiment, the smaller pores (a few 100 nm), which are due to voids in the carbon black–binder network, are not taken into account in the simulation. However, considering the simplifications made, a good overall estimation of the pore diameter could be made by the simulation.

In summary, it could be shown that both the scaling approach for the simulation speed and the simulation approach in its entirety can be considered valid for different areal loading without representing the fluid phase via a CFD–DEM coupling. In the long term, however, the possibility should be created to take different particle shapes into account.

## 10. Conclusion and Outlook

A simulation setup has been developed that is capable of predicting the development of electrode thickness and density during the drying process. This requires a single calibration of the simulated carbon black porosity and the friction coefficients within a formulation and process route. In preliminary studies, it has been shown that the achieved film thickness is highly dependent on the adjusted carbon black porosity and friction coefficients, with higher friction coefficients and carbon black porosities leading to higher final film thicknesses. A good agreement between the simulated layer thicknesses and the experiment has been reached for different areal loadings. The setup is based on the DEM and avoids coupling with a CFD simulation using surrogate models for the relevant fluid effects like buoyancy, Stokes friction, lubrication, and capillary forces. The basis for this was a precise investigation of the effects occurring during drying. Also, a different distinction between carbon black, binder, and solvent has been made contrary to existing approaches.

The next steps in the further development of the approach should include a deeper validation of the generated structure and its transport properties like in other studies.<sup>[20,21]</sup> Here, synchrotron or nano-CT measurements are conceivable, which enable to evaluate the solid volume fraction along with the layer thickness and, thus, further validate the obtained structure. In the future, nonspherical particles should also be considered.

A central point when it comes to evaluating the drying process of battery electrodes is the binder distribution. The presented approach forms a good basis for the complete mapping of the drying process by means of DEM simulations. A logical further development would be the coupling with a model that describes the binder distribution. It would be conceivable to use the temporal change of the porosity of the electrode along the layer thickness, for example, to locally and temporally resolve diffusion coefficients in binder modeling.

Furthermore, a coupling with a DEM-based calendaring simulation is aimed at, which uses the electrode structure from the drying simulation as input parameters.

## Appendix A

**Table A1.** Material properties and dryer characteristics utilized for the determination of the drying rates.

Quantity	Value	Unit	Source
Dryer			
Number of zones × length	3 × 2	M	Own measurement
Heat transfer coefficient zone 1	40	W m <sup>-2</sup> K <sup>-1</sup>	Own measurement
Heat transfer coefficient zone 2	40	W m <sup>-2</sup> K <sup>-1</sup>	Own measurement
Heat transfer coefficient zone 3	55	W m <sup>-2</sup> K <sup>-1</sup>	Own measurement
Material properties NMP at 100 °C			
Heat capacity gas <sup>a)</sup>	133.3	J mol <sup>-1</sup> K <sup>-1</sup>	[56]
Heat capacity liquid <sup>a)</sup>	185.2	J mol <sup>-1</sup> K <sup>-1</sup>	[56]
Molar mass	0.09913	kg mol <sup>-1</sup>	–
Vapor pressure <sup>a)</sup>	2976	Pa	[55]
Evaporation heat <sup>a)</sup>	51 008	J mol <sup>-1</sup>	[55]

<sup>a)</sup>These quantities are implemented as a function of temperature. The exact equations are obtained from the respective source.

## Acknowledgements

The authors gratefully acknowledge the financial support by the Federal Ministry for Education and Research (BMBF) within the research project “Sim4Pro” (03XP0242A). Furthermore, the authors would like to thank Alexander Diener and Michael Bredekamp for providing electrode data and Christine Burmeister and Silas Wolf for their valuable assistance.

Open Access funding enabled and organized by Projekt DEAL.

## Conflict of Interest

The authors declare no conflict of interest.

## Data Availability Statement

The data that support the findings of this study are available from the corresponding author upon reasonable request.

## Keywords

batteries, cathodes, discrete element method, drying, electrodes

Received: July 6, 2022

Revised: August 18, 2022

Published online:

- [1] A. Kwade, W. Haselrieder, R. Leithoff, A. Modlinger, F. Dietrich, K. Droeder, *Nat. Energy* **2018**, *3*, 290.
- [2] H. Dreger, H. Bockholt, W. Haselrieder, A. Kwade, *J. Electron. Mater.* **2015**, *44*, 4434.
- [3] H. Bockholt, W. Haselrieder, A. Kwade, *ECS Trans.* **2013**, *50*, 25.
- [4] V. Wenzel, H. Nirschl, D. Nötzel, *Energy Technol.* **2015**, *3*, 692.

- [5] L. S. Kremer, A. Hoffmann, T. Danner, S. Hein, B. Prifling, D. Westhoff, C. Dreer, A. Latz, V. Schmidt, M. Wohlfahrt-Mehrens, *Energy Technol.* **2020**, *8*, 1900167.
- [6] S. Jaiser, A. Friske, M. Baunach, P. Scharfer, W. Schabel, *Drying Technol.* **2016**, *35*, 1266.
- [7] M. Stein, A. Mistry, P. P. Mukherjee, *J. Electrochem. Soc.* **2017**, *164*, A1616.
- [8] M. Baunach, S. Jaiser, S. Schmelzle, H. Nirschl, P. Scharfer, W. Schabel, *Drying Technol.* **2015**, *34*, 462.
- [9] C. Meyer, M. Kosfeld, W. Haselrieder, A. Kwade, *J. Energy Storage* **2018**, *18*, 371.
- [10] C. F. Oladimeji, P. L. Moss, M. H. Weatherspoon, *Adv. Chem.* **2016**, *2016*, 1.
- [11] R. Sim, S. Lee, W. Li, A. Manthiram, *ACS Appl. Mater. Interfaces* **2021**, *13*, 42898.
- [12] B. Westphal, H. Bockholt, T. Gunther, W. Haselrieder, A. Kwade, *ECS Trans.* **2015**, *64*, 57.
- [13] F. Font, B. Protas, G. Richardson, J. M. Foster, *J. Power Sources* **2018**, *393*, 177.
- [14] T. Lombardo, J.-B. Hoock, E. N. Primo, A. C. Ngandjong, M. Duquesnoy, A. A. Franco, *Batteries Supercaps* **2020**, *3*, 721.
- [15] M. M. Forouzan, C.-W. Chao, D. Bustamante, B. A. Mazzeo, D. R. Wheeler, *J. Power Sources* **2016**, *312*, 172.
- [16] A. Rucci, A. C. Ngandjong, E. N. Primo, M. Maiza, A. A. Franco, *Electrochim. Acta* **2019**, *312*, 168.
- [17] A. C. Ngandjong, A. Rucci, M. Maiza, G. Shukla, J. Vazquez-Arenas, A. A. Franco, *J. Phys. Chem. Lett.* **2017**, *8*, 5966.
- [18] M. Chouchane, A. Rucci, T. Lombardo, A. C. Ngandjong, A. A. Franco, *J. Power Sources* **2019**, *444*, 227285.
- [19] T. Lombardo, A. C. Ngandjong, A. Belhacen, A. A. Franco, *Energy Storage Mater.* **2021**, *43*, 337.
- [20] A. C. Ngandjong, T. Lombardo, E. N. Primo, M. Chouchane, A. Shodiev, O. Arcelus, A. A. Franco, *J. Power Sources* **2021**, *485*, 229320.
- [21] I. Srivastava, D. S. Bolinteanu, J. B. Lechman, S. A. Roberts, *ACS Appl. Mater. Interfaces* **2020**, *12*, 34919.
- [22] C. Sangrós Giménez, B. Finke, C. Nowak, C. Schilde, A. Kwade, *Adv. Powder Technol.* **2018**, *29*, 2312.
- [23] C. Sangrós Giménez, B. Finke, C. Schilde, L. Froböse, A. Kwade, *Powder Technol.* **2019**, *349*, 1.
- [24] C. Sangrós Giménez, C. Schilde, L. Froböse, S. Ivanov, A. Kwade, *Energy Technol.* **2019**, *217*, 1900180.
- [25] S. Jaiser, J. Kumberg, J. Klaver, J. L. Urai, W. Schabel, J. Schmatz, P. Scharfer, *J. Power Sources* **2017**, *345*, 97.
- [26] J. C. Eser, B. Deichmann, T. Wirsching, L. Merklein, M. Müller, P. Scharfer, W. Schabel, *Drying Technol.* **2022**, *40*, 1130.
- [27] G. Trefalt, M. Borkovec, *Overview of DLVO Theory*, University of Geneva, Geneva **2014**.
- [28] M. Zhu, J. Park, A. M. Sastry, *J. Electrochem. Soc.* **2011**, *158*, A1155.
- [29] F. Ma, Y. Fu, V. Battaglia, R. Prasher, *J. Power Sources* **2019**, *438*, 226994.
- [30] S. H. Sung, S. Kim, J. H. Park, J. D. Park, K. H. Ahn, *Materials* **2020**, *13*, 4544.
- [31] K. Y. Cho, Y. I. Kwon, J. R. Youn, Y. S. Song, *Mater. Res. Bull.* **2013**, *48*, 2922.
- [32] Y. I. Kwon, J. D. Kim, Y. S. Song, *J. Electron. Mater.* **2015**, *44*, 475.
- [33] M. Ishii, H. Nakamura, *JCIS Open* **2022**, *6*, 100048.
- [34] M. Kroupa, M. Vonka, M. Soos, J. Kosek, *Langmuir* **2016**, *32*, 8451.
- [35] P. A. Cundall, O. D. L. Strack, *Géotechnique* **1979**, *29*, 47.
- [36] S. S. Kumar, Z. He, C. J. Hogan, S. A. Fredericks, J. Hong, *Meas. Sci. Technol.* **2020**, *31*, 125201.
- [37] J. Grubbs, K. Tsaknopoulos, C. Massar, B. Young, A. O'Connell, C. Walde, A. Birt, M. Siopis, D. Cote, *Powder Technol.* **2021**, *391*, 20.
- [38] J. Mayer, H. Bockholt, A. Kwade, *Inner Carbon Black Porosity as Characteristic Parameter for the Microstructure of Lithium-Ion Electrodes and its Effect on Physical and Electrochemical Properties* **2022**.
- [39] T. Roessler, A. Katterfeld, *Particuology* **2019**, *45*, 105.
- [40] H. C. Hamaker, *Physica* **1937**, *4*, 1058.
- [41] S. L. Dance, M. R. Maxey, *J. Comput. Phys.* **2003**, *189*, 212.
- [42] O. I. Vinogradova, *Langmuir* **1995**, *11*, 2213.
- [43] B. Finke, A. Kwade, C. Schilde, *Materials* **2020**, *13*, 4288.
- [44] I. M. Krieger, T. J. Dougherty, *Trans. Soc. Rheol.* **1959**, *3*, 137.
- [45] T. Breinlinger, T. Kraft, *Powder Technol.* **2014**, *256*, 279.
- [46] Y. T. Feng, D. R. J. Owen, *Comp. Part. Mech.* **2014**, *1*, 159.
- [47] Y. T. Feng, J. Loughran, *Eng. Comput.* **2009**, *26*, 599.
- [48] A. Diener, S. Ivanov, W. Haselrieder, A. Kwade, *Energy Technol.* **2022**, *10*, 2101033.
- [49] L. Froboese, P. Titscher, B. Westphal, W. Haselrieder, A. Kwade, *Mater. Charact.* **2017**, *133*, 102.
- [50] S. Jaiser, M. Müller, M. Baunach, W. Bauer, P. Scharfer, W. Schabel, *J. Power Sources* **2016**, *318*, 210.
- [51] J. Kumberg, M. Müller, R. Diehm, S. Spiegel, C. Wachsmann, W. Bauer, P. Scharfer, W. Schabel, *Energy Technol.* **2019**, *7*, 1900722.
- [52] J. Kumberg, M. Baunach, J. C. Eser, A. Altvater, P. Scharfer, W. Schabel, *Energy Technol.* **2021**, *9*, 2000889.
- [53] J. Kumberg, M. Baunach, J. C. Eser, A. Altvater, P. Scharfer, W. Schabel, *Energy Technol.* **2021**, *9*, 2100013.
- [54] C. Meyer, M. Weyhe, W. Haselrieder, A. Kwade, *Energy Technol.* **2019**, *11*, 1900175.
- [55] "Dortmund Data Bank", www.ddbst.com (accessed: Feb 2022).
- [56] *McGraw-Hill's AccessEngineering* (Ed: C. L. Yaws), McGraw-Hill Education; McGraw Hill, New York, NY **1999**.